Partially etched $Bi_2O_2CO_3$ by metal chloride for enhanced reactive oxygen species generation: A tale of two strategies

Penghui Ding[a,1], Jun Di[b,1], Xiaoliu Chen[a], Junze Zhao[a], Kaizhi Gu[c], Yi Zhang[a], Sheng Yin[a], Gaopeng Liu[a], Jiexiang Xia[a,*], Huaming Li[a,*]

[a] School of Chemistry and Chemical Engineering, Institute for Energy Research, Jiangsu University, 301 Xuefu Road, Zhenjiang, 212013, PR China
[b] Center for Programmable Materials, School of Materials Science & Engineering, Nanyang Technological University, Singapore 639798, Singapore
[c] School of Chemistry and Molecular Engineering, East China University of Science and Technology, Shanghai 200237, PR China

ARTICLE INFO

ABSTRACT

Light-mediated reactive oxygen species generation with water and oxygen is generally regarded as a mild and efficient way for organic pollutants removal. However, it is highly difficult but desirable to construct a photochemical system with increased reactive oxygen species production. Herein, by using $Bi_2O_2CO_3$ as a prototype, we devise a simple metal chloride-involved etching method to achieve better light absorption and charge carriers separation in a wide-band-gap semiconductor, thus giving rise to improved molecular oxygen activation. The improved photoinduced reactive oxygen species production is further verified by excellent photocatalytic degradation ability of RhB, TC and BPA under visible and ultraviolet light illumination. In addition, the metal chloride-induced strategies—heterojunction formation and cation doping—significantly affect the dynamics and transfer of carriers, which are advantageous to manipulate one-/two-electron pathway for producing reactive oxygen species.

1. Introduction

Reactive oxygen species (ROS), such as superoxide ion ($\cdot O_2^-$), hydroxyl radical ($\cdot OH$) and hydrogen peroxide (H_2O_2), play crucial roles in many fields—pollutants elimination, organic synthesis and artificial photosynthesis. [1–3] Generally, ROS can be generated through physical processes (sonolysis or radiolysis), chemical reactions (electrochemical or photochemical reactions) and biological methods (oxidative phosphorylation) [4–6]. Of all the processes or methods above, activation of molecular oxygen by accepting electrons from conduction band (CB) or lowest unoccupied molecular orbital (LUMO) of a semiconductor upon sunlight irradiation is unequivocally considered to be the most used and cheapest method. [1,7] Due to the kinetically persistent or spin-forbidden nature of triplet ($3\Sigma_g^-$) ground state molecular oxygen, the efficiency of molecular oxygen activation often falls far short of expectations. [8,9] It is widely acknowledged that light-involved molecular oxygen activation is directly related to the complicated coupling process involving photons, hot carriers (electrons and holes) and neutral excitons (electron − hole pair), which is depend on the optoelectronics and charge carrier mobility of a semiconductor. [10,11] Thus, it is of paramount importance to find some easy yet

effective methods so as to engineer the optoelectronic and charge transfer properties of a semiconductor.

In recent years, many groups have succeeded in developing some approaches to the above problems. These approaches can be roughly classified as pure semiconductor engineering or material coupling. The former method mainly involves doping, facet engineering, defect engineering and structure regulation of the pure semiconductor. [12] Chen et al. firstly demonstrated that doping-induced defect engineering method could bring about significant changes in the crystal structure of a semiconductor, which was beneficial for producing ROS for pollutants removal and bacteria inactivation [13]. Zhang and coworkers combined the facet engineering and vacancy engineering methods for sustainable oxygen activation in an oxygen vacancies (OVs)-containing {001} facet exposed BiOCl, displaying better performance than that of the benchmark TiO_2 under solar light. [14] Ye's group reported that 2D nanostructure and carbon-doping could synergistically enhance ROS generation in bismuth molybdate material, thus leading to better performance towards NO removal [7]. The latter method mostly focuses on coupling with other semiconductor, metal or even insulator. [15,16] Li and coworkers modified g-C_3N_4 with semiconductor ZnO and insulator Al_2O_3 to facilitate cascading electron transportation, resulting
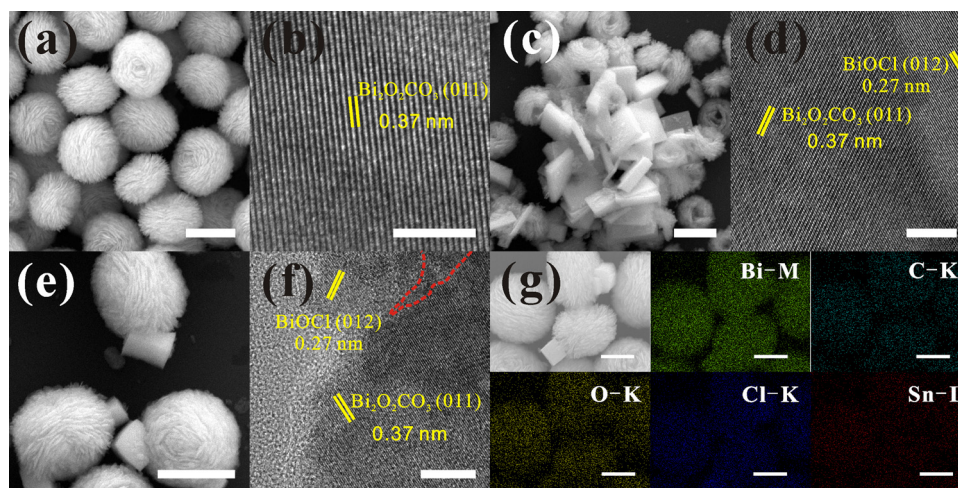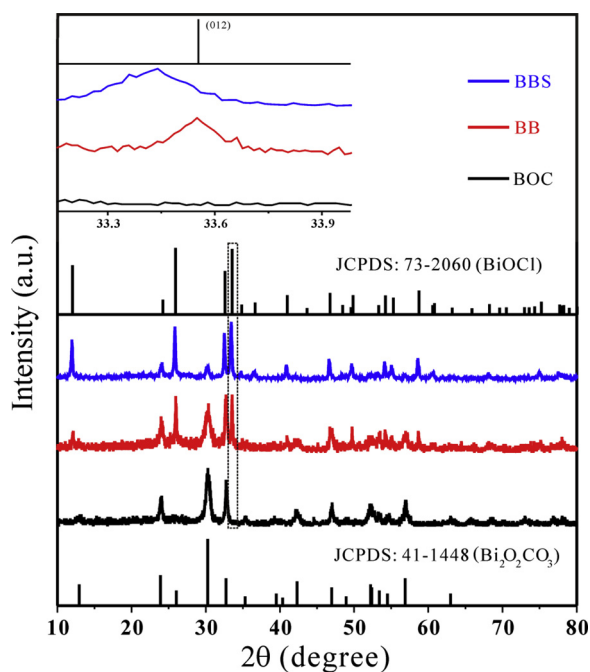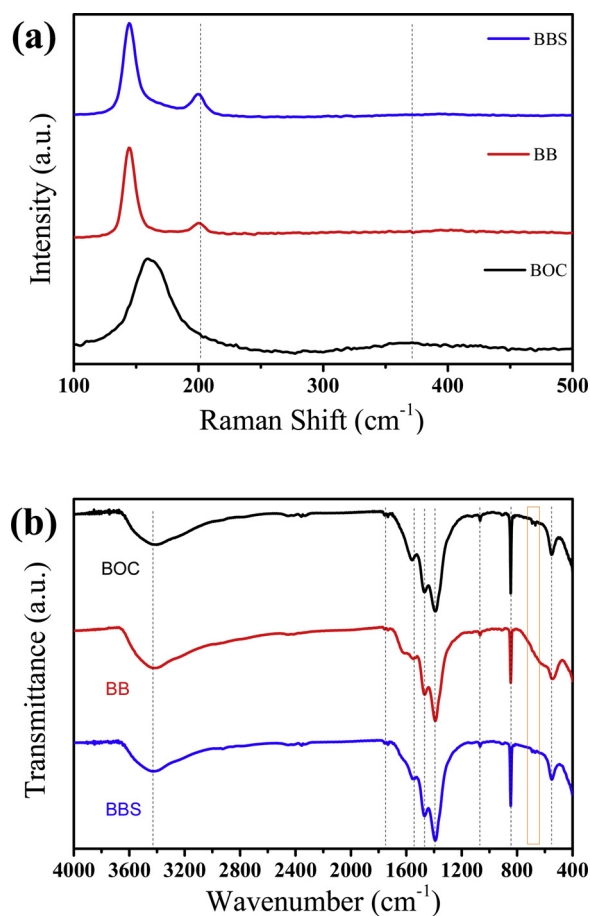

Fig. 1. (a, c, e) SEM images of BOC, BB and BBS samples. Scale bars, 1 μm. (b, d, f) HRTEM images of BOC, BB and BBS samples. Scale bars, 5 nm, 5 nm, 10 nm, respectively. (g) SEM image of BBS and corresponding elemental mapping. Scale bars, 0.5 μm.

Fig. 2. XRD patterns of pure BOC, BB and BBS samples.

Fig. 3. (a) Raman and (b) FT-IR spectra of pure BOC, BB and BBS samples.

in higher concentration of $\cdot O_2^-$ and $\cdot OH$. [17] Many groups employed nanosized metal (Au, Ag) to suppress hot carriers recombination or induce surface plasmon resonance (SPR) effect for improving ROS generation even under near infrared irradiation [18–21]. Despite enormous efforts invested in tuning band structure and pathway of carriers, it is still difficult to develop a simple and even general method, which integrates the two approaches above, for ROS production.

As a member of famous Aurivillius phase oxides, $Bi_2O_2CO_3$ consists of alternate $[Bi_2O_2]^{2+}$ and CO_3^{2-} layers, and the two layers are orthogonal to each other. Due to intrinsic large structure distortion and layered structure, $Bi_2O_2CO_3$ usually exhibits better photocatalytic ability than that of TiO_2 under same condition. [22] Nonetheless, like TiO_2, the efficiency of photochemical reaction is largely limited by narrow light absorbance and rapid carriers recombination, which are harmful for ROS generation. However, to the best of our knowledge, there are rare reports regarding molecular-oxygen-activation-related ROS generation on $Bi_2O_2CO_3$, let alone detailed analysis of ROS production pathway.

In this work, we employ highly hydrolysable stannous chloride ($SnCl_2$) to partially etch $Bi_2O_2CO_3$, thus resulting in heterojunction formation and cation doping (Sn-doped $BiOCl/Bi_2O_2CO_3$) at the same time. The etched $Bi_2O_2CO_3$ shows enhanced ROS generation because of increased one-/two-electron reactions, which leads to improved RhB, TC and BPA degradation under visible and UV light. We also investigate formation mechanisms in detail, which might be favorable for wide utilization of this method for increasing ROS production.
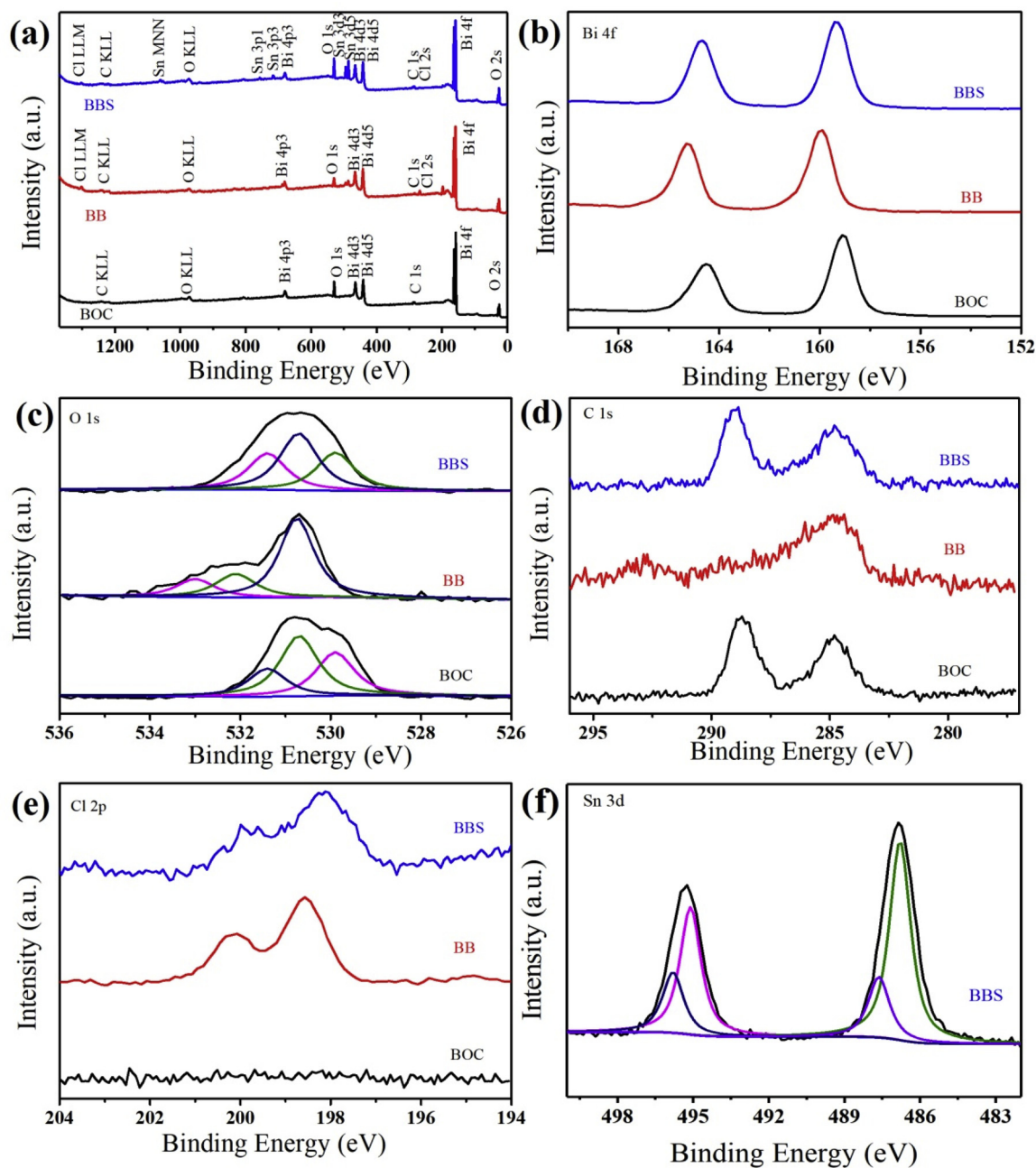
Fig. 4. XPS spectra of BOC, BB, BBS samples. (a) survey, (b) Bi 4f, (c) O 1s, (d) C 1s, (e) Cl 2p and (f) Sn 3d.

2. Experimental section

2.1. Reagents and chemicals

Sodium carbonate (Na_2CO_3, 99.8%), stannous chloride ($SnCl_2 \cdot 2H_2O$, 98%), hydrochloric acid (HCl, 36%~38%), ethanol (C_2H_6O, 97%), potassium chloride (KCl, 99.5%), sodium chloride (NaCl, 99.5%), hydrogen peroxide (H_2O_2, 30% w/w aqueous), terephthalic acid ($C_8H_6O_4$, 99%), nitro blue tetrazolium ($C_{40}H_{30}Cl_2N_{10}O_6$, 98%), ammonium oxalate ($C_2H_8N_2O_4 \cdot H_2O$, 99.5%), benzoquinone ($C_6H_4O_2$, 98%), potassium dichromate ($K_2Cr_2O_7$, 99.8%), tert-Butanol ($C_4H_{10}O$, 98%), isopropanol (C_3H_8O, 99.7%), sodium sulfate (Na_2SO_4, 99%), ethylenediaminetetraacetic acid ($C_{10}H_{14}N_2Na_2O_8 \cdot 2H_2O$, 97%) and RhB ($C_{28}H_{31}ClN_2O_3$, AR) were purchased from Sinopharm Chemical Reagent Co. Ltd. BPA ($C_{15}H_{16}O_2$, 99%) and iron sulfate ($FeSO_4$, 99%) were purchased from Aladdin. TC ($C_{22}H_{24}N_2O_8 \cdot HCl$,

USP) was kindly supplied by Macklin. Bismuth(III) citrate ($C_6H_5BiO_7$, 99.99%) and Nafion (10% wt%) were purchased from Sigma-Aldrich. [C_{16}MIm]Cl ($C_{20}H_{39}ClN_2$, 99%) was obtained from Shanghai Chengjie Chemical Co. Ltd. High purity nitrogen (N_2, 99.999%) was from Zhenjiang Zhongpu Steel Materials Co. Ltd. All reagents and chemicals were directly used without any purification processes. Deionized (DI) water was used in all experiments.

2.2. Materials synthesis

Fabrication of pure $Bi_2O_2CO_3$: In a typical procedure, 4 mmol of bismuth(III) citrate and 4 mmol of sodium carbonate were dissolved in 70 mL of DI water under vigorous magnetic stirring for 30 min. Then the mixed solution was introduced into a Teflon-lined autoclave and heated at 160 °C for 48 h. The obtained white precipitates were centrifuged, washed with DI water and absolute ethanol for three times and
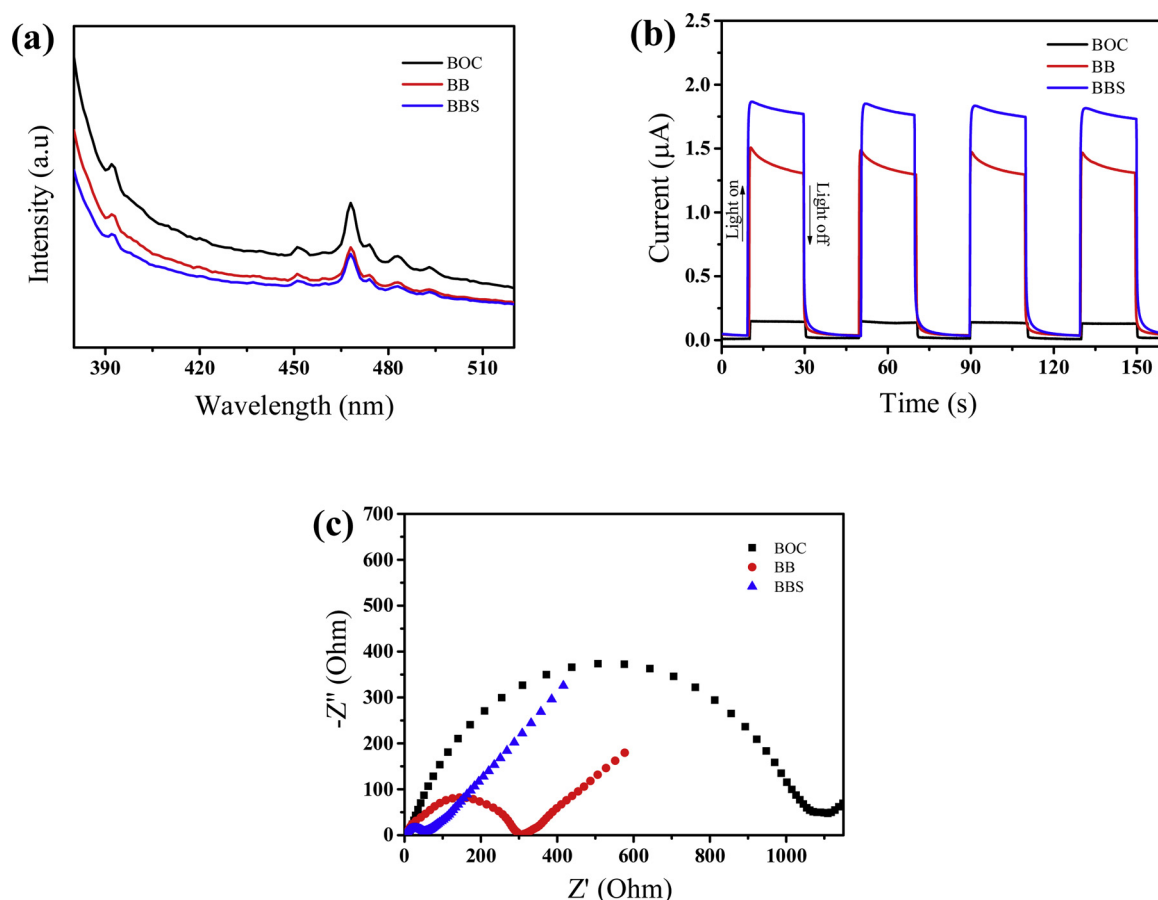
Fig. 5. (a) PL spectra, (b) photocurrent and (c) EIS plots of BOC, BB and BBS.

dried at 60 °C for 12 h. The final products were denoted as BOC.

Fabrication of partially etched $Bi_2O_2CO_3$ by metal chloride: Typically, 16 mg of stannous chloride was added in a mixed solution containing 20 mL of DI water and 20 mL of ethanol under vigorous magnetic stirring for 10 min. Then 0.2 g of as-prepared BOC was slowly added in above mixed solution and subject to vigorous magnetic stirring for 1 h. Finally, the turbid solution was poured into a Teflon-lined autoclave and treated at 120 °C for 6 h. The obtained products were centrifuged, washed with DI water and absolute ethanol for three times and dried at 60 °C for 12 h. The final products (Sn-doped BiOCl/ $Bi_2O_2CO_3$) were denoted as BBS.

Fabrication of etched $Bi_2O_2CO_3$ by hydrochloric acid: In a typical procedure, 0.3 mL of hydrochloric acid was added in a mixed solution containing 20 mL of DI water and 20 mL of ethanol under vigorous magnetic stirring. Then 0.2 g of as-prepared BOC was slowly added in above mixed solution and subject to vigorous magnetic stirring for 1 h. Finally, the turbid solution was poured into a Teflon-lined autoclave and treated at 120 °C for 6 h. The obtained products were centrifuged, washed with DI water and absolute ethanol for many times and dried at 60 °C for 12 h. The final products (BiOCl/$Bi_2O_2CO_3$) were denoted as BB.

2.3. Characterizations

X-ray diffraction (XRD) analysis was performed on a Shimadzu XRD-6000 diffractometer in the range of 10-80°at a scanning rate of 7°/min. The nanostructures were characterized by scanning electron microscope (JEOL, JSM-7001 F) and transmission electron microscope (Tecnai, G2 F30 S-TWIN). Fourier transform infrared (FT-IR) spectra were obtained on a Nexus 470 FT-IR spectrophotometer. Raman spectra were acquired on a Raman spectroscope (Renishaw Invia). X-ray

photoelectron spectroscopy (XPS) measurements were conducted on VG MultiLab 2000. The specific surface area and pore structure were determined by TriStar II 3020 Surface Area and Porosity Analyzer. Ultraviolet − visible (UV − vis) diffuse reflectance spectra (DRS) were acquired on a Shimadzu UV-2450 spectrometer. The photoluminescence (PL) properties were determined by a Varian Cary Eclipse spectrometer. Electron spin resonance (ESR) signals were obtained on a Bruker JES-FA200 spectrometer. The photocurrent and electrochemical impedance spectroscopy (EIS) measurements were performed on a CHI 660E electrochemical workstation.

2.4. Photocatalytic degradation ability

The photocatalytic activity was evaluated by photodegradation of RhB (10 mg L^{-1}), TC (20 mg L^{-1}), and BPA (10 mg L^{-1}) under visible and UV light. A 300 W Xenon lamp with a filter to cut off UV light ($\lambda > 400$ nm) and a 250 W high pressure mercury lamp were employed as visible and UV light source, respectively. 25 mg, 50 mg, and 100 mg of catalyst were added in the pollutants solution (100 ml) of RhB, TC and BPA, respectively. The pollutants solution was first vigorously stirred for 30 min to achieve adsorption–desorption equilibrium. During the whole process, air was constantly pumped into the reaction system. At specific intervals, 3 ml of the mixture was sampled and centrifuged for further analysis. The photocatalytic performance of the catalysts was determined by the methods used in our previous report.[23]
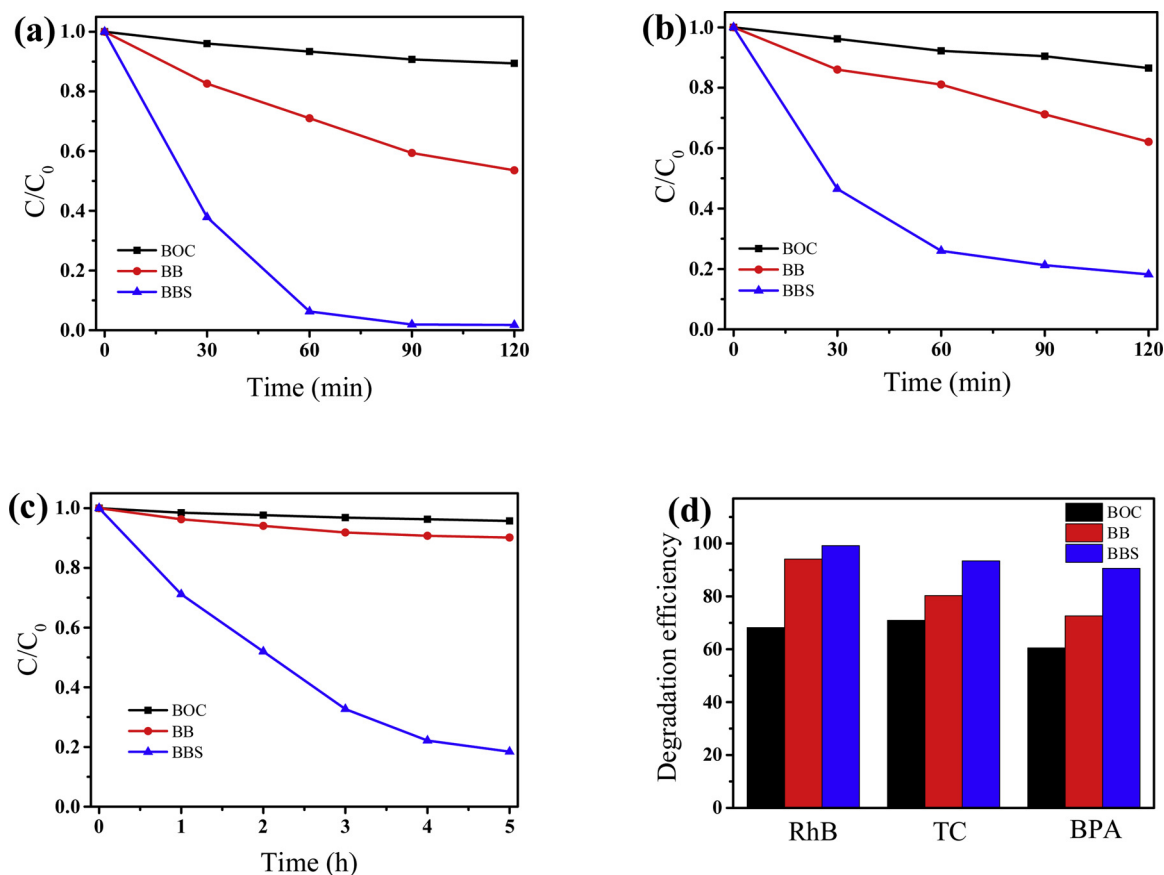
Fig. 6. Photocatalytic experiments of (a) RhB, (b) TC and (c) BPA removal by BOC, BB and BBS samples under visible light. (d) Photocatalytic experiments of RhB, TC and BPA elimination by BOC, BB and BBS samples under UV light.
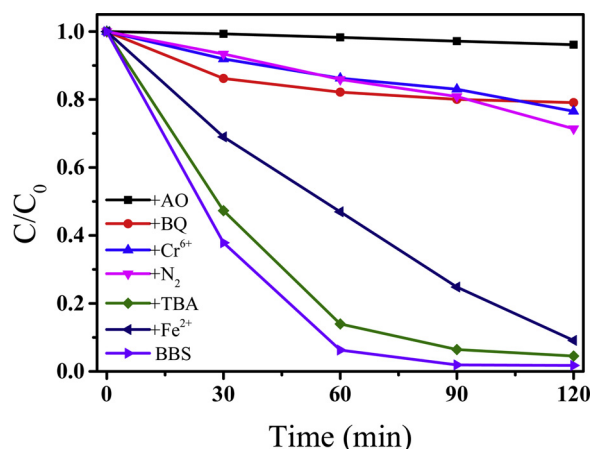

Fig. 7. Effects of different scavengers on the photocatalytic activity of RhB degradation.

3. Result and discussion

3.1. Formation mechanism and morphology investigation

It is very difficult to obtain $BiOCl/Bi_2O_2CO_3$ heterostructure directly from $Bi_2O_2CO_3$ precursor in that carbonate ions (CO_3^{2-}) can bind with BiO^+ ions more strongly than Cl^- ions. [24] Currently, the appropriate way to prepare $BiOCl/Bi_2O_2CO_3$ heterostructure from $Bi_2O_2CO_3$ is to add HCl solution into the precursor, since $Bi_2O_2CO_3$ can be etched by HCl followed by releasing BiO^+ and the BiO^+ subsequently reacts with Cl^- ions to form BiOCl. [25] However, this method is unsafe

(hydrochloric acid is highly corrosive) and difficult to control (the amount and injection speed of hydrochloric acid should be carefully maintained). Even worse, most existed $BiOCl/Bi_2O_2CO_3$ hybrids by this method are only UV-responsive, resulting in low molecular oxygen activation efficiency. [26–29] Given that $SnCl_2$ tends to release H^+ owning to the highly hydrolysable nature among many metal chlorides, it is expected that the heterostructure might be formed as in the case of hydrochloric acid. [30,31] After adding $Bi_2O_2CO_3$ into the $SnCl_2$ mixture solution, the $Bi_2O_2CO_3$ is partially etched with the release of BiO^+. Then the Sn complex and Cl^- ions produced by proper hydrolysis of $SnCl_2$ can bind with BiO^+ to turn into Sn-doped BiOCl under solvothermal condition. [32] To fully determine the heterostructure formation process, time-dependent SEM images are performed. As seen in **Fig. S1a**, the pure BOC displays a uniform rose-like hierarchical structure with a diameter of 1 μm. After reacting for 1 h or 2 h (**Fig. S1b, c**), some broken sheets, which might serve as growth nuclei, are present in the vicinity of BOC probably due to the fact that hydrolysable $SnCl_2$ could etch pure BOC. Then the broken sheets are self-assembled into Lego-like nanoplates on pure BOC, suggesting an intimate contact with BOC (3 h, **Fig. S1d**). [33] Further prolonging reaction time (5–6 h, **Fig. S1e, f**) will result in more nanoplates, because more H^+ consumption might lead to more H^+ generation (Le Chatelier's principle). [34] It should be noted that the overall 3D nanostructure of BOC is preserved over the entire process possibly owing to the proper choose of chlorine source and reaction medium. We also replace $SnCl_2$ with other chlorine sources (KCl, [C_{16}MIm]Cl and NaCl) to highlight the importance of hydrolysis. According to **Fig. S2a**, the XRD patterns of KCl/[C_{16}MIm]Cl/NaCl-treated samples are as nearly same as that of pure BOC, and the degradation performance (**Fig. S2b**) of these products also remains the same. The results above demonstrate the importance of proper select of a hydrolysable chlorine source. We further conduct a
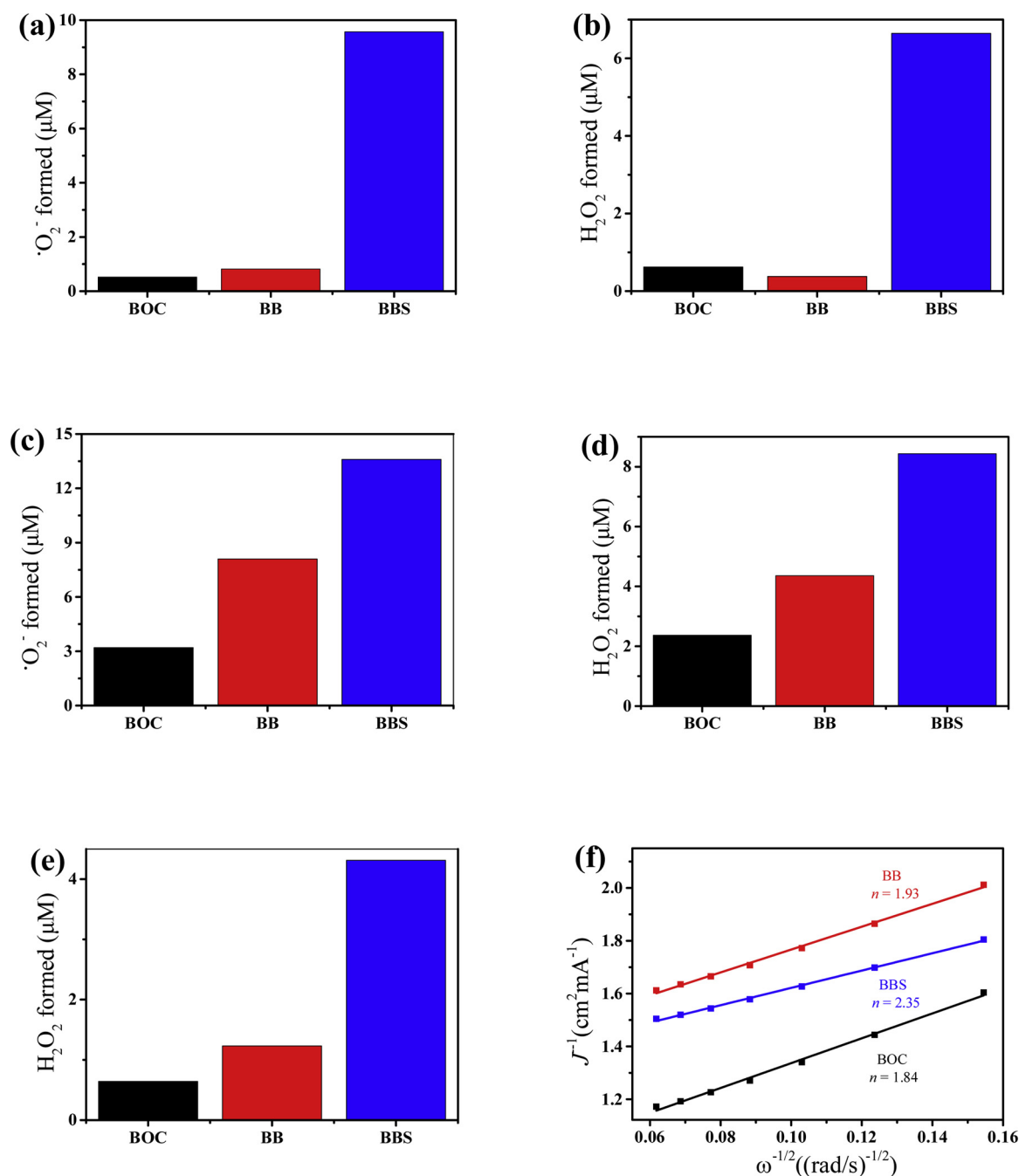
Fig. 8. Photocatalytic production of $\cdot O_2^-$ or H_2O_2 in the presence of BOC, BB and BBS samples under (a, b) visible and (c, d) UV light. (e) H_2O_2 evolution over BOC, BB and BBS in the presence of NBT. (f) Koutecký-Levich plots at 0.4 V *vs.* RHE of BOC, BB and BBS catalysts.

series of experiments using different reaction media. When adding pure water or ethanol, the morphologies of pure BOC are destroyed or entirely without variation, respectively (**Fig. S3a, b**). This might be because the hydrolysis rate of $SnCl_2$ in water is much faster than that of in ethanol, indicating that proper hydrolysis rate is vital for the morphology control (**Fig. S3d**). [35] In order to further investigate the role of hydrolysable chlorine source, we conduct TEM experiments. As shown in Fig. 1a, b, the pure BOC shows a flower-like nanostructure with a continuous lattice spacing of 0.373 nm, which agrees with the (011) plane of BOC. [36] After etching directly by pure HCl, the whole morphology of BOC is significantly changed since HCl will release copious H^+ ions immediately. The existence of heterojunction can be easily verified by the two different lattice fringes (Fig. 1c, d), corresponding to the (011) plane of BOC (0.37 nm) and (012) plane BiOCl

(0.27 nm). However, the morphology of BOC (Fig. 1e) is well retained by employing $SnCl_2$ and water-ethanol mixture as metal chlorine source or reaction medium. Compared with HCl-etching method, the atomic structure of metal chloride-etching product is changed significantly. The HRTEM of BBS (Fig. 1f) displays not only typical (011) plane and (012) plane of BOC and BiOCl, but also a disordered area (encircled by red dashed line) between BOC and BiOCl. This disordered area might be the synergistic effect of lattice mismatch between the interfaces and doping, further resulting in lattice distortion or lattice strain. [37] These results are consistent with many emerging nanocatalysts for photo(electro)catalysis. [38,39] Elemental mapping (Fig. 1g) also indicates the homogeneous presence of relevant elements (Bi, C, O, Cl and Sn) in BBS.
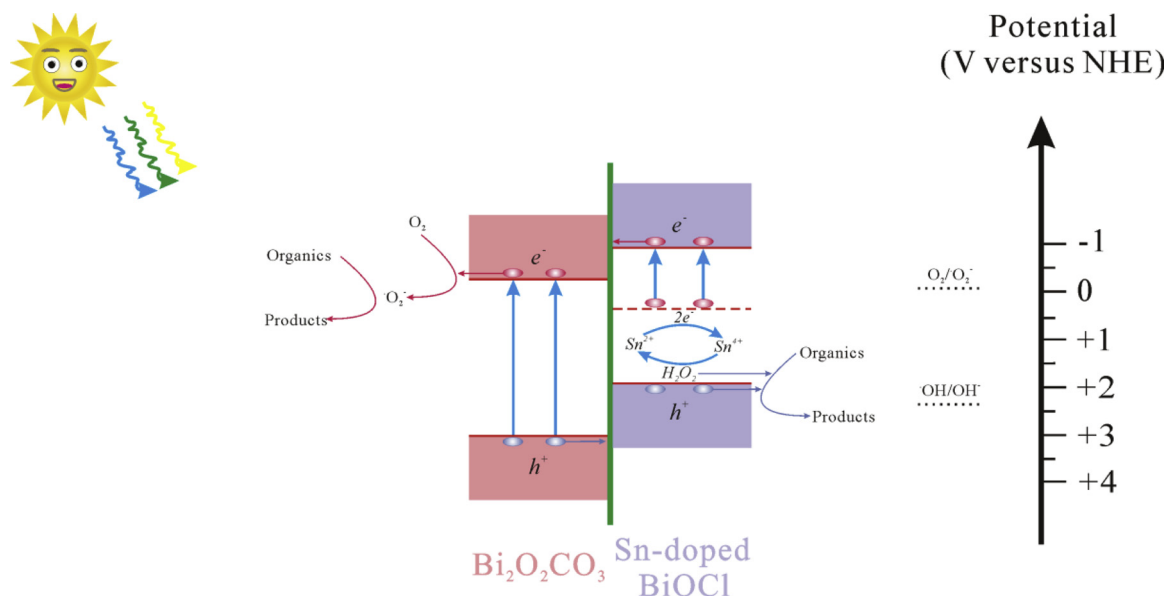
Fig. 9. Scheme of ROS generation for pollutants degradation under light irradiation.

3.2. Compositional and structural information

X-ray diffraction (XRD) patterns of pure $Bi_2O_2CO_3$ (BOC), BiOCl/$Bi_2O_2CO_3$ (BB) and Sn-doped BiOCl/$Bi_2O_2CO_3$ (BBS) are shown in Fig. 2. All three samples exhibit sharp diffraction peaks similar to their standard PDF card ($Bi_2O_2CO_3$: 41–1488; BiOCl: 73–2060). However, the amplified XRD result shows that the (012) peak of BiOCl in BBS shifts to lower degree. The subtle change might be attributed to the fact that the ionic radius of Sn^{2+} (1.12 Å) is larger than that of Bi^{3+} (1.03 Å), demonstrating the Sn atoms have been doped into the lattice of BiOCl. [13,40] Moreover, the amplified XRD patterns of $Bi_2O_2CO_3$ (**Fig. S4**) display that the crystal structure of $Bi_2O_2CO_3$ in BBS is not affected after the introduction of $SnCl_2$.

In order to further understand the effect of heterojunction formation and heteroatom doping into crystal structure, Raman and FT-IR measurements are then carried out. It can be seen from Raman spectra (Fig. 3a) that the weak band at $ca.$ 367 cm^{-1} of BOC, which can be assigned to the external vibration of Bi-O bond, nearly disappears after treating with HCl and $SnCl_2$, suggesting the partial etching of $Bi_2O_2CO_3$. [41] In addition, the strong peak at roughly 161 cm^{-1} of BOC, which can be attributed to the vibration modes of the carbonate ion, shifts to lower wavenumber, which is also indicative of heterojunction formation. [27] Notably, the newly formed peak at 201 cm^{-1} of BB, which is the typical stretching mode of E_g internal Bi-Cl in BiOCl, shifts to lower wavenumber in BBS, evidencing the significant crystal distortion of BiOCl after Sn doping. [13] A weak band located at 670 cm^{-1} of FT-IR spectra (Fig. 3b) of BOC can be observed, which can be ascribed to the in-plane deformation of carbonate ion. Moreover, the peak nearly disappear after etching by HCl, further signifying etching of BOC. However, the band reappears after treating with $SnCl_2$, which is the typical Sn-O stretching mode possibly arising from replacement of bismuth atoms with tin atoms. [42] These findings indicate the formation of heterojunction and heteroatom doping by metal chloride, and subsequently affect the BOC matrix and BiOCl.

XPS is employed to reveal the surface states of BOC, BB and BBS, further illuminating the effect of metal chloride-involved etching method. The survey spectrum (Fig. 4a) accurately indicates the presence of Bi, C, O, Cl and Sn elements in these catalysts. The peaks at 164.4 eV and 159.1 eV of BOC (Fig. 4b) correspond to Bi $4f_{5/2}$ and Bi $4f_{7/2}$ of trivalent bismuth ion (Bi^{3+}), respectively. [43] After treating directly by HCl, Bi^{3+} peaks of BB shift to higher binding energy due to formation of heterojunction. [44] However, the peaks of BBS exhibit a lower binding energy shift compared with BB sample due to the fact that the electronegativity of Bi (2.02) is slightly larger than that of Sn (1.96) [45]. These differences also demonstrate the successful formation of heterojunction and implantation of Sn. The effect of metal chloride-involved etching method is further elaborated by similar positive or negative shifts of O 1 s, C 1 s and Cl 2p core levels (Fig. 4c–e). The Sn 3d spectrum of BBS (Fig. 4f) can be deconvoluted into four peaks, signifying the coexistence of 2 + and 4 + oxidation states of Sn. This can be ascribed to the partial transformation of Sn^{2+} to Sn^{4+}, and the conversion process is well documented in recent researches of tin-containing perovskite photovoltaics. [46–49]

The nitrogen adsorption − desorption isotherms of BOC, BB and BBS materials (**Fig. S5a-c**) show that the surface areas of BB and BBS materials remain nearly the same after treating with HCl and $SnCl_2$, respectively. From the above results, we might conclude that the enhancement of catalytic activity is not directly correlated with the surface area [50].

3.3. Photo(electro)chemical properties

The change in the composition and crystal structure of a semiconductor can unavoidably affect dynamics and transfer of carriers (h$^+$-e$^-$ pairs), further inducing substantial difference in catalytic activity of a semiconductor photocatalyst. [51] As shown in Fig. 5a, the steady-state PL intensity of BBS is lower than that of pure BOC and BB samples, illustrating that the two strategies can effectively inhibit the recombination of hot carriers and facilitate the redox reactions. Moreover, BBS displays higher and stable photocurrent (Fig. 5b) than that of BB owning to the introduction of Sn^{2+}/Sn^{4+} redox couple. On the contrary, pure BOC shows the lowest photocurrent since pure BOC suffers from narrow visible light absorption and low h$^+$-e$^-$ pairs separation rate arising from intrinsic drawbacks. The arc radius (Fig. 5c) of Nyquist plot of BBS is the smallest among these samples, indicating low interfacial charge transfer resistance of BBS, which may be beneficial for related photochemical applications [52].

3.4. Photocatalytic activities and stability tests of the composites

The photocatalytic activities of the as-obtained samples are measured by photodegradation of model pollutants. As shown in **Fig. S6a**, the photolysis experiments indicate the pollutants are relatively stable under light irradiation without catalysts. The degradation efficiency of

BBS (Fig. 6a) is significantly better than that of BOC or BB samples under visible light irradiation. Pure BOC does not show notable degradation performance towards RhB removal due to limited light absorption. However, the degradation efficiency can reach *ca.* 40% after treating with HCl possibly due to indirect dye sensitization. [53] In contrast, BBS can eliminate roughly 90% of RhB in 60 min due to the simultaneous formation of heterojunction and ion doping. According to the kinetic fit curve (**Fig. S7a**), the BBS catalyst possesses the highest rate constant of $0.0384 \, min^{-1}$, which is nearly 7 or even 38 times higher than that of BB or BOC, respectively. To further test the photooxdation ability of the as-synthetized samples, we try to use the catalysts to remove TC and BPA. Similar to the result above, the BBS has the best photocatalytic performance towards TC and BPA degradation. About 80% TC and BPA (Fig. 6b, c) can be removed by BBS in 2 h or 5 h. However, BOC and BB samples can barely degrade the non-dye pollutants (antibiotics: TC; endocrine-disrupting chemicals: BPA) under visible light due to the lack of dye photosensitization. The superiority of metal chloride-involved etching method can be also confirmed by corresponding linear fit curves (**Fig. S7b, c**) of TC and BPA degradation process. The rate constant for TC or BPA removal of BBS is about 14 or 8 times higher than that of pure BOC, respectively. Total organic carbon (TOC) experiment is conducted to reveal mineralization capability for degradation of RhB by BBS under visible light irradiation. As shown in **Fig. S7d**, 46% of RhB is mineralized after irradiation for 120 min, and it shows that RhB can be degraded by BBS under visible light irradiation. The photocatalytic activity of relevant samples (such as Sn-doped BiOCl) is also presented in **Fig. S8a-c**, and the results still manifest that the combined strategies are beneficial for photooxidation reactions. To test the catalyst's ability for practical application in large-scale pollutants removal, recycling experiments are carried out. The experiments results (**Fig. S9a**) display that the BBS catalyst is relatively stable after 5 consecutive cycles, and the XRD patterns (**Fig. S9b**) before and after photocatalysis also support the above result. Moreover, it is rather surprising to find that the BBS catalyst even shows better degradation performance under UV light (Fig. 6d). Many wide-band-gap photocatalysts suffer from reduced oxidative activity after doping under UV light even they show enhanced photoactivity under visible light due to increased photoabsorption in visible region. [54] However, the oxidative activity of $Bi_2O_2CO_3$ is retained and even enhanced probably due to the unique formation of heterostructure and cation doping by one-step metal chloride etching method.

3.5. Mechanisms analysis of enhanced reactive oxygen species generation

To ascertain the ROS involvement in the process, we conduct several scavenging experiments. According to Fig. 7, the photocatalyst cannot remove pollutant after adding ammonium oxalate (AO), indicating the importance of holes (h^+) in the degradation process. Similarly, only 20% of RhB can be degraded in the presence of superoxide radical scavengers (benzoquinone (BQ) or N_2), and it shows that $\cdot O_2^-$ also plays a critical role in photocatalytic oxidation reactions. After adding a powerful H_2O_2 scavenger (Fe^{2+}), the rate constant for RhB removal is smaller than that of BBS, evidencing certain role of H_2O_2 in the decolorization process. [55] We further add Cr^{6+} as electron (e^-) scavenger into the photoreaction system, and find that the photocatalytic reaction cannot proceed as well. This might ascribe to the fact that degradation process is strongly related to the photoinduced ROS, which can be produced by electron-involved molecular oxygen activation. However, the degradation performance remains nearly the same after addition of tert-Butanol (TBA), signaling the minor role of $\cdot$OH. The production of relevant ROS is further verified by electron spin resonance (ESR). As seen in **Fig. S10a**, the BBS displays typical 1:1:1:1 spin adducts ESR spectra, which is indicative of superoxide radical anion formation. However, the typical ESR spectra for DMPO-$\cdot$OH (**Fig. S10b**) cannot be found, which are consistent with scavenging experiments for hydroxyl radical.

To clarify the importance of the metal chloride-induced strategies in enhancing ROS generation, we measure the concentration of superoxide radical anion and hydrogen peroxide under visible and UV light irradiation. As expected, the pure BOC and BB catalysts are reluctant to produce oxygen-related species under visible light irradiation due to limited light absorption. However, the BBS catalyst shows better molecular oxygen activation (Fig. 8a, b) due to the implantation of heteroatoms. Under UV light irradiation, the concentration of photoinduced $\cdot O_2^-$ of BBS is about 4 or 2 times higher than that of BOC or BB, respectively (Fig. 8c). The better $\cdot O_2^-$ generation by one-electron molecular oxygen activation of BBS catalyst can be further demonstrated by the color change (purple) of the photoreaction system after experiments (**Fig. S11a, b**). Similarly, the concentration of photoinduced H_2O_2 of BBS (Fig. 8d) is still higher than that of BOC or BB under UV light. The above results show the increased ROS generation of BBS catalyst by metal chloride-involved etching method. To fully understand the H_2O_2 generation pathway, we add NBT into the reaction system to suppress the one-electron, two-step O_2 reduction to H_2O_2 ($O_2 \rightarrow \cdot O_2^- \rightarrow H_2O_2$). As shown in Fig. 8e, the H_2O_2 evolution of pure BOC and BB is significantly affected. However, the BBS catalyst can still produce certain amount of hydrogen peroxide. It is generally believed that H_2O_2 could be generated by one-electron pathway or two-electron pathway, therefore the above result implies that the BBS sample might have the two-electron route to produce H_2O_2. According to some recent reports about redox couple-related photocatalysts, we surmise that the Sn^{2+}/Sn^{4+} redox couple might facilitate the two-electron reaction for H_2O_2 production: $2H^+ + O_2 + Sn^{2+} \rightarrow Sn^{4+} + H_2O_2$. [13,56] To gain more insights into the whole process, we conduct rotating disk electrode (RDE) experiments. As seen in Fig. 8f, the average number of electrons involved in the O_2 reduction process by BOC or BB is 1.84 and 1.93, respectively, suggesting the presence of one-electron O_2 reduction. On the contrary, the BBS might catalyze two-electron reaction (n = 2.35) to produce H_2O_2 due to the introduction of tin atoms even if the one-electron pathway is blocked by the introduction of NBT. The aforementioned analyses indicate the combined strategies promote the excellent ROS production of the BBS catalyst.

The optical property of the as-obtained samples is evaluated by DRS and Mott-Schottky plots. The pure BOC, as a typical UV-responsive semiconductor, has a band gap of 3.31 eV. In contrast, Sn-doped BiOCl (denoted by BiOClS) displays much enhanced light absorption in the range of visible light, corresponding to a band gap of 2.91 eV (**Fig. S13a**). The flat band positions (V_{fb}) of BOC and Sn-doped BiOCl can be determined by Mott-Schottky analysis. According to **Fig. S13b**, the V_{fb} positions of BOC and Sn-doped BiOCl are –0.23 and -0.88 V *vs.* NHE, respectively. Considering the typical difference between the V_{fb} position and conduction band (CB) edge of an n-type semiconductor is 0-0.1 V, the CBEs of BOC and Sn-doped BiOCl are -0.28 and -0.93 V *vs.* NHE, respectively. [57] Based on the results above, the valence band (VB) edges of BOC and Sn-doped BiOCl are 3.03 and 1.98 V *vs.* NHE, respectively. Therefore, a possible ROS production pathway for photodegradation of organic pollutants is presented in Fig. 9. Upon sunlight irradiation, the pure BOC or BiOClS could both generate electron-hole pairs. In our case, the electrons from VB are transferred to the Sn-doping energy level of BiOClS due to the conversion between the Sn^{2+}/Sn^{4+} redox couple. Then the electrons from the doping level are excited by sunlight and transferred to the CB of BiOClS. Finally, the electrons in the CB of BiOClS might transfer to the CB of BOC owing to the different band structures. And the photogenerated holes in the VB of pure BOC are transferred to BiOClS. The accumulated electrons in the CB of BOC then react with molecular oxygen to form superoxide ions for removing pollutants, and the holes in BiOClS are directly used to attack organics. It is worth mentioning that enhanced hydrogen peroxide production might be due to the *in situ* generated redox couple, thereby contributing to the degradation performance.

4. Conclusions

The current work focuses on the use of a hydrolysable metal chloride to partially etch a typical UV-responsive semiconductor ($Bi_2O_2CO_3$) for increased ROS ($\cdot O_2^-$ and H_2O_2) generation. Benefitting from the two strategies (heterojunction formation and cation doping) in one 'tale', the intrinsic UV-light-driven $Bi_2O_2CO_3$ displays good photoactivity in the visible range and even better photocatalytic removal of pollutants under UV light. The reason for the positive change in the photocatalytic performance is the successful manipulation of one-/two-electron pathway for ROS generation. This investigation on metal chloride-mediated ROS generation of $Bi_2O_2CO_3$ might be extended to other wide–band-gap semiconductors for relevant applications.

Acknowledgement

Appendix A. Supplementary data

Supplementary material related to this article can be found, in the online version, at doi:https://doi.org/10.1016/j.apcatb.2018.12.047.

References

[1] H.W. Huang, S.T. Tu, C. Zeng, T.R. Zhang, A.H. Reshak, Y.H. Zhang, Angew. Chem., Int. Ed. 56 (2017) 11860–11864.
[2] S. Zavahir, Q. Xiao, S. Sarina, J. Zhao, S. Bottle, M. Wellard, J.F. Jia, L.Q. Jing, Y.M. Huang, J.P. Blinco, H.S. Wu, H.-Y. Zhu, ACS Catal. 6 (2016) 3580–3588.
[3] B. Tian, B.N. Tian, B. Smith, M.C. Scott, R.N. Hua, Q. Lei, Y. Tian, Nat. Commun. 9 (2018) 1397.
[4] G.Z. Xu, M.R. Chance, Chem. Rev. 107 (2007) 3514–3543.
[5] S. Gligorovski, R. Strekowski, S. Barbati, D. Vione, Chem. Rev. 115 (2015) 13051–13092.
[6] M. Hayyan, M.A. Hashim, I.M. AlNashef, Chem. Rev. 116 (2016) 3029–3085.
[7] S.Y. Wang, X. Ding, X.H. Zhang, H. Pang, X. Hai, G.M. Zhan, W. Zhou, H. Song, L.Z. Zhang, H. Chen, J.H. Ye, Adv. Funct. Mater. 27 (2017) 1703923.
[8] W.T. Borden, R. Hoffmann, T. Stuyver, B. Chen, J. Am. Chem. Soc. 139 (2017) 9010–9018.
[9] M. Metz, E.I. Solomon, J. Am. Chem. Soc. 123 (2001) 4938–4950.
[10] H. Wang, S.C. Chen, D.Y. Yong, S.C. Zhang, S. Li, W. Shao, X.S. Sun, B.C. Pan, Y. Xie, J. Am. Chem. Soc. 139 (2017) 4737–4742.
[11] H. Wang, D.Y. Yong, S.C. Chen, S.L. Jiang, X.D. Zhang, W. Shao, Q. Zhang, W.S. Yan, B.C. Pan, Y. Xie, J. Am. Chem. Soc. 140 (2018) 1760–1766.
[12] H. Yi, L. Qin, D.L. Huang, G.M. Zeng, C. Lai, X.G. Liu, B.S. Li, H. Wang, C.Y. Zhou, F.L. Huang, S.Y. Liu, X.Y. Guo, Chem. Eng. J. 358 (2019) 480–496.
[13] Z. Dai, F. Qin, H.P. Zhao, J. Ding, Y.L. Liu, R. Chen, ACS Catal. 6 (2016) 3180–3192.
[14] H. Li, J.G. Shi, K. Zhao, L.Z. Zhang, Nanoscale 6 (2014) 14168–14173.
[15] H. Yi, D.L. Huang, L. Qin, G.M. Zeng, C. Lai, M. Cheng, S.J. Ye, B. Song, X.Y. Ren, X.Y. Guo, Appl. Catal. B 239 (2018) 408–424.
[16] H. Yi, G.M. Zeng, C. Lai, D.L. Huan, L. Tang, J.L. Gong, M. Chen, X. Piao, H. Wang, M. Cheng, C. Zhang, W.P. Xiong, Chem. Eng. J. 330 (2017) 134–145.
[17] S.J. Liu, F.T. Li, Y.L. Li, Y.J. Hao, X.J. Wang, B. Li, R.H. Liu, Appl. Catal. B 212 (2017) 115–128.
[18] C.H. Fang, H.L. Jia, S. Chang, Q.F. Ruan, P. Wang, T. Chen, J.F. Wang, Energy Environ. Sci. 7 (2014) 3431–3438.
[19] W.W. He, H.K. Kim, W.G. Wamer, M. David, H.C. John, J.J. Yin, J. Am. Chem. Soc. 136 (2014) 750–757.
[20] N. Waiskopf, Y. Ben-Shahar, M. Galchenko, I. Carmel, G. Moshitzky, H. Soreq, U. Banin, Nano Lett. 16 (2016) 4266–4273.
[21] J. Di, J.X. Xia, M.X. Ji, B. Wang, S. Yin, Y. Huang, Z.G. Chen, H.M. Li, Appl. Catal. B 188 (2016) 376–387.
[22] Y. Zheng, F. Duan, M.Q. Chen, Y. Xie, J. Mol. Catal. A Chem. 317 (2010) 34–40.
[23] J. Di, J.X. Xia, Y.P. Ge, H.P. Li, H.Y. Ji, H. Xu, Q. Zhang, H.M. Li, M.N. Li, Appl. Catal. B 168-169 (2015) 51–61.
[24] A. Etogo, E. Hu, C.M. Zhou, Y.J. Zhong, Y. Hu, Z.L. Hong, J. Mater. Chem. A 3 (2015) 22413–22420.
[25] J. Cao, X. Li, H.L. Lin, S.F. Chen, X.L. Fu, J. Hazard. Mater. 239–240 (2012) 316–324.
[26] J. Cao, X. Li, H.L. Lin, B.Y. Xu, S.F. Chen, Q.M. Guan, Appl. Surf. Sci. 266 (2013) 294–299.
[27] H.J. Lu, L.L. Xu, B. Wei, M.Y. Zhang, H. Gao, W.J. Sun, Appl. Surf. Sci. 303 (2014) 360–366.
[28] X. Zhang, T. Guo, X. Wang, Y. Wang, C. Fan, H. Zhang, Appl. Catal. B 150–151 (2014) 486–495.
[29] L.H. Yu, X.Y. Zhang, G.W. Li, Y.T. Cao, Y. Shao, D.Z. Li, Appl. Catal. B 187 (2016) 301–309.
[30] Z.Y. Wang, D.Y. Luan, F.Y.C. Boey, X.W. Lou, J. Am. Chem. Soc. 133 (2011) 4738–4741.
[31] C.F. Baes, R.E. Mesmer, The Hydrolysis of Cations, Wiley-Interscience, New York, 1976.
[32] Y.F. Jiang, J.C. Hu, J.L. Li, RSC Adv. 6 (2016) 39810–39817.
[33] J. Di, J.X. Xia, Y.P. Ge, L. Xu, H. Xu, M.Q. He, Q. Zhang, H.M. Li, J. Mater. Chem. A 2 (2014) 15864–15874.
[34] L.C. Buelens, V.V. Galvita, H. Poelman, C. Detavernier, G.B. Marin, Science 354 (2016) 449–452.
[35] Y. Yang, D.M. Ma, T. Cheng, Y.H. Gao, G.H. Li, NANO 10 (2015) 1550087-1-9.
[36] F. Dong, T. Xiong, Y.J. Sun, H.W. Huang, Z.B. Wu, J. Mater. Chem. A 3 (2015) 18466–18474.
[37] M.C. Luo, S.J. Guo, Nat. Rev. Mater. 2 (2017) 17059.
[38] J. Di, J. Xiong, H.M. Li, Z. Liu, Adv. Mater. 30 (2018) 1704548.
[39] L.Z. Bu, N. Zhang, S.J. Guo, X. Zhang, J. Li, J.L. Yao, T. Wu, G. Lu, J.-Y. Ma, D. Su, X.Q. Huang, Science 354 (2016) 1410–1414.
[40] V.B.R. Boppana, R.F. Lobo, J. Catal. 281 (2011) 156–168.
[41] Y. Wu, Q.F. Han, L. Wang, X. Wang, J.W. Zhu, Mater. Chem. Phys. 187 (2017) 72–81.
[42] X.X. Xu, J. Zhuang, X. Wang, J. Am. Chem. Soc. 130 (2008) 12527–12535.
[43] L. Chen, J. He, Q. Yuan, Y. Liu, C.-T. Au, S.-F. Yin, J. Mater. Chem. A 3 (2015) 1096–1102.
[44] L.M. Sun, L. Xiang, X. Zhao, C.J. Jia, J. Yang, Z. Jin, X.F. Cheng, W.L. Fan, ACS Catal. 5 (2015) 3540–3551.
[45] A.L. Allred, J. Inorg. Nucl. Chem. 17 (1961) 215–221.
[46] F. Hao, C.C. Stoumpos, P. Guo, N. Zhou, T.J. Marks, R.P.H. Chang, M.G. Kanatzidis, J. Am. Chem. Soc. 137 (2015) 11445–11452.
[47] W. Ke, C.C. Stoumpos, J.L. Logsdon, M.R. Wasielewski, Y. Yan, G. Fang, M.G. Kanatzidis, J. Am. Chem. Soc. 138 (2016) 14998–15003.
[48] K.P. Marshall, M. Walker, R.I. Walton, R.A. Hatton, Nat. Energy 1 (2016) 16178.
[49] T.-B. Song, T. Yokoyama, C.C. Stoumpos, J. Logsdon, D.H. Cao, M.R. Wasielewski, S. Aramaki, M.G. Kanatzidis, J. Am. Chem. Soc. 139 (2017) 836–842.
[50] J. Di, C. Zhu, M.X. Ji, M.L. Duan, R. Long, C. Yan, K.Z. Gu, J. Xiong, Y.B. She, J.X. Xia, H.M. Li, Z. Liu, Angew. Chem. Int. Ed. 57 (2018) 14847–14851.
[51] L. Chen, R. Huang, M. Xiong, Q. Yuan, J. He, J. Jia, M.-Y. Yao, S.-L. Luo, C.-T. Au, S.-F. Yin, Inorg. Chem. 52 (2013) 11118–11125.
[52] B.S. Li, C. Lai, G.M. Zeng, L. Qin, H. Yi, D.L. Huan, C.Y. Zhou, X.G. Liu, M. Cheng, P. Xu, C. Zhang, F.L. Huang, S.Y. Liu, ACS Appl. Mater. Interfaces 10 (2018) 18824–18836.
[53] J. Jiang, K. Zhao, X.Y. Xiao, L.Z. Zhang, J. Am. Chem. Soc. 134 (2012) 4473–4476.
[54] J.M. Herrmann, New J. Chem. 36 (2012) 883–890.
[55] W.J. Wang, T.W. Ng, W.K. Ho, J.H. Huang, S.J. Liang, T.C. An, G.Y. Li, J.C. Yu, P.K. Wong, Appl. Catal. B 129 (2013) 482–490.
[56] M.Y. Xing, W.J. Xu, C.C. Dong, Y.C. Bai, J.B. Zeng, Y. Zhou, J.L. Zhang, Y.D. Yin, Chemistry 4 (2018) 1359–1372.
[57] J. Shang, W.C. Hao, X.J. Lv, T.M. Wang, X.L. Wang, Y. Du, S.X. Dou, T.F. Xie, D.J. Wang, J.O. Wang, ACS Catal. 4 (2014) 954–961.